Drag-free Control and Drag Force Recovery of Small Satellites

Anh N. Nguyen
NASA Ames Research Center
NASA Ames Research Center, M/S 202-3, Bldg N202, Moffett Field, CA 93035
anh.n.nguyen@nasa.gov

John W. Conklin
University of Florida
[Second Author Address]; (650) 308-6351
jwconklin@ufl.edu

ABSTRACT

Drag-free satellites provide autonomous precision orbit determination, accurately map the static and time varying components of Earth's mass distribution, aid in our understanding of the fundamental force of gravity, and will ultimately open up a new window to our universe through the detection and observation of gravitational waves. At the heart of this technology is a gravitational reference sensor, which (a) contains and shields a free-floating proof mass from all non-gravitational forces, and (b) precisely measures the position of the test mass inside the sensor. Thus, both test mass and spacecraft follow a pure geodesic in spacetime. By tracking the position of a low Earth orbiting drag-free satellite we can directly determine the detailed shape of geodesics and through analysis, the higher order harmonics of the Earth's geopotential. This paper explores two different drag-free control systems on small satellites. The first drag-free control system is a continuously compensated single thruster 3-unit CubeSat with a suspension-free spherical proof-mass. A feedback control system commands the thruster and Attitude and Determination Control System to fly the "tender" spacecraft with respect to the test mass. The sphere's position is sensed with a LED-based differential optical shadow sensor, its electric charge controlled by photoemission using UV LEDs, and the spacecraft position is maintained with respect to the sphere using an ion electrospray propulsion system. This configuration is the most fuel-efficient drag-free system possible today. The second drag-free control system is an electro-statically suspended cubical proof-mass that is operated with a low duty cycle, limiting suspension force noise over brief, known time intervals on a small GRACE-II -like satellite. The readout is performed using a laser interferometer, which is immune to the dynamic range limitations of voltage references. This system eliminates the need for a thruster, enabling drag-free control systems for passive satellites. In both cases, the test mass position, GPS tracking data, and commanded actuation, either thrust or suspension system, can be analyzed to estimate the 3-axis drag forces acting on the satellite. The data produces the most precise maps of upper atmospheric drag forces and with additional information, detailed models that describe the dynamics of the upper atmosphere and its impact on all satellites that orbit the Earth. This paper highlights the history, applications, design, laboratory technology development and highly detailed simulation results of each control system.

MOTIVATION

Precision accelerometry and drag-free systems provide measurements of upper atmospheric winds and density distribution, accurately map the static and time varying components of Earth's mass distribution, and can ultimately open up a new window to the universe through the detection and observation of gravitational waves. At the heart of this technology is a gravitational reference sensor, which (a) contains and shields a free-floating proof mass from all non-gravitational forces, and (b) precisely measures the position of the proof mass inside the sensor. Traditional accelerometry is performed using an electrostatic accelerometer which contains a high-density cubic proof mass, surrounded by an electrode housing. The housing has an electrostatic suspension system that capacitively senses and actuates the proof mass. Drag-free systems directly cancel non-gravitational forces acting on a spacecraft by flying in formation with the proof mass, so that both proof mass and spacecraft follow a pure geodesic. This paper explores two novel techniques for drag-free control systems and disturbance force recovery on small satellites. The drag-free system utilizes a single thruster 3-unit (3U) CubeSat with a suspension-free spherical proof mass. A feedback control system commands the thruster and attitude and determination control system to fly the 'tender' spacecraft with respect to the proof mass. The sphere's position is sensed with a light emitting diode-based differential

optical shadow sensor and the spacecraft position is maintained with respect to the sphere using an ion electrospray propulsion system. Since fuel is used to directly compensate for the disturbance force, this configuration is the most fuel-efficient drag-free system possible. The second drag-free system is a hybrid accelerometer/drag-free system called a drift-mode accelerometer. Like classical accelerometers, this instrument uses an electrostatically suspended cubic proof mass inside an electrode housing. Unlike traditional accelerometers, its proof mass suspension system is operated on a low duty cycle, limiting the suspension force noise to brief and known time intervals. This system has the potential to achieve drag-free acceleration noise performance without the need for a thruster or drag-free control. In both drag-free systems, the test mass position, global positioning system tracking data, and commanded actuation, can be analyzed to estimate the 3-axis disturbance forces acting on the satellite.

Drag-free technology is useful for a broad range of applications, listed in Table 1, which are separated into four distinct categories: 1) navigation, 2) Earth science, 3) fundamental physics, and 4) astrophysics. Each of these categories requires a specific drag-free performance and a metrology performance metric. The drag-free performance metric is the residual acceleration of the PM in units of meters per second-squared per square-root Hertz ($ms^{-2}Hz^{-1/2}$). An ideal drag-free spacecraft would have a residual acceleration of zero, but in practice, small residual forces act on the PM and perturb its trajectory from a pure geodesic. Therefore, the primary goal of the drag-free spacecraft design is to minimize these residual forces. The metrology performance metric is the measurement of the absolute position of a drag-free PM (e.g. via global positioning system (GPS)) for a single spacecraft or the differential measurement of the distance between two drag-free PMs for spacecraft pairs. Under both circumstances, the goal of the metrology design is to maintain the measurement noise below a required level.

In navigation applications, drag-free technology enables precise orbit determination and autonomous orbit maintenance. When non-gravitational forces are cancelled, the exact orbit of the spacecraft can be estimated more accurately because the relatively large uncertainties associated with atmospheric drag and solar radiation pressure can be eliminated from the equations of motion governing the spacecraft dynamics. In addition, orbit corrections can be made continuously, simplifying operations. In a NASA Earth Science Technology Office Study on drag-free technology, drag-free systems are found to reduce fuel consumption by 50% and reduce navigation error by 30% – 50% in a

comparison between a continuously drag-compensated system and one corrected once after 4 weeks at a 350 km altitude. The potential of substantial cost savings enables constellations of spacecraft to be both feasible and achievable in orbits with substantial drag.

Table 1:   Summary of drag-free applications

Category	Application	Performance ($ms^{-2}\ Hz^{-1/2}$)	Metrology
Navigation	Autonomous, fuel-efficient orbit maintenance	$\leq 10^{-10}$, near zero frequency[1]	≤ 10 m absolute
	Precision real-time on-board navigation	$\leq 10^{-10}$, near zero frequency[1]	≤ 10 m absolute
Earth Science	Aeronomy	$\leq 10^{-10}$, 10^{-2} to 1 Hz	1 m absolute
	Geodesy	10^{-10}, 10^{-2} to 1 Hz[2]	10^{-5} mHz$^{-1/2}$ differential
	Future Earth Geodesy	$\leq 10^{-10}$, 10^{-2} to 1 Hz*	$\leq 10^{-9}$ mHz$^{-1/2}$ differential
Fundamental Physics	Equivalence Principle Tests	$\leq 10^{-10}$, 10^{-2} to 1 Hz[28]	$\leq 10^{-10}$ mHz$^{-1/2}$ differential
	Tests of General Relativity	$\leq 10^{-10}$, near zero frequency[4]	≤ 1 m absolute
Astrophysics	Gravitational Waves	$3\ 10^{-15}$, 10^{-4} to 1 Hz[7]	$\leq 10^{-11}$ differential

In geodesy applications, drag-free technology allows for fine-structured gravity field maps of the Earth and other planetary bodies. By removing all non-gravitational disturbances in real-time, the drag-free system simplifies the data analysis and allows for improved performance by reducing the dynamic range of the measurement. Since the desired acceleration measurements of the spacecraft due to small-scale mass fluctuations on the Earth have magnitudes on the order of 1×10^{-12} ms^{-2} and drag forces acting on the spacecraft can have magnitudes on the order of 1×10^{-6} ms^{-2}, an accelerometer with a dynamic range of at least 10^6 is required. Drag-free operations on the other hand, cancel the drag force directly, eliminating the need for a high dynamic range measurement. With drag-free spacecraft, differential measurements between two geodesics can be performed more accurately (e.g. using laser interferometry). This can be used to improve measurements made by NASA's twin Gravity Recovery and Climate Experiment (GRACE) satellites, which have been in orbit since 2002. [1,2] Higher resolution gravity field maps from future drag-free missions can

divulge the complex interactions between the atmosphere and the biosphere. These maps can be integrated with other disciplines such as geophysics, oceanography, and atmospheric studies, to contribute to the overall understanding of the impact of global climate change.

Lastly, the same drag-free technology can aid our understanding of the fundamental force of gravity. Through the nature of the drag-free spacecraft, the PM is subjected to a pure free-fall, exposing effects of gravity that can be measured and studied precisely. By measuring the differential acceleration of a pair of drag-free PMs that are nominally co-located, one can search for violations of the equivalence of inertial and gravitational mass.[3] By placing drag-free spacecraft into orbits experiencing relatively high gravitational potentials (e.g. near the Sun)[4] or relatively low gravitational potential (e.g. Lagrange points)[5] one can perform other tests of General Relativity[6]. Subsequently, drag-free technologies will ultimately be able to detect and observe gravitational waves.[7]

To date, four drag-free missions have flown: Triad I with its DISturbance Compensation System (DISCOS) in 1972, along with several follow-on missions, National Aeronautics and Space Administration's (NASA) Gravity Probe B (GP-B) in 2004, European Space Agency's (ESA) Gravity field and steady-state Ocean Circulation Explorer (GOCE) in 2009, and the Laser Interferometer Space Antenna Path Finder (LPF) in 2015. The first drag-free system, DISCOS, was implemented by the U.S. Navy Triad program and achieved a drag-free performance of better than 10^{-10} ms^{-2} (RMS) over 10-day periods. Triad I and DISCOS extended the time required for ephemeris updates to several weeks.[8] Since then, GP-B confirmed two effects of Einstein's 1916 general theory of relativity by measuring the geodetic and frame-dragging effects using ultra-precise gyroscopes in low Earth orbit.[3] The ESA's GOCE mission used 6 electrostatic accelerometers to form a 3-axis gravity gradiometer, which measured the Earth's static gravity field to a high spatial order.[9] GOCE used a single-axis drag-free system to reduce the dynamic range requirement for the electrostatic accelerometers. In the near future, the Microscope[6] mission will test the weak equivalence principal to 10^{-15}, and the LISA Pathfinder mission will demonstrate differential acceleration noise between a pair of PMs to below 3×10^{-14} ms^{-2}Hz$^{-1/2}$.[10]

Electrostatic accelerometers (EA) are traditionally used for spacecraft accelerometry. An EA consists of a free-floating high-density PM housed by an electrostatic suspension system. The inner PM is centered in its housing via continuous electrostatic forcing. The accuracy of an EA is limited by the voltage reference stability of the electrostatic suspension system. The most precise electrostatic accelerometers commercially available are capable of measuring spacecraft acceleration relative to the inertial frame to ~10^{-11} ms^{-2}Hz$^{-1/2}$ from roughly 1 mHz to 1 Hz, and produced by ONERA[6]. Drag-free systems provide more accurate acceleration measurements over traditional EAs, and are operated in two modes.

The first drag-free mode is 'accelerometer' mode, where an EA is used as the primary sensor and a propulsion system on the exterior of the spacecraft is used to minimize the suspension force needed to keep the PM centered in its housing. This drag-free mode directly counters the disturbance forces acting on the spacecraft and reduces the nominal voltage applied to the housing electrodes, thus reducing the electrostatic force noise. Therefore, the accuracy of the acceleration measurement is improved. By pairing a mass spectrometer to the system, the contributions of density and atmospheric wind to the total disturbance force can also be determined. Measurements of the upper atmospheric drag are continually useful in improving mathematical models and orbit determination. The GP-B, GOCE, and Microscope missions have implemented accelerometer drag-free mode.

The second drag-free operating mode is 'true' drag-free, where the electrostatic suspension force is turned completely off, in at least in one degree of freedom. The PM measurement is the primary sensor and the propulsion system on the exterior of the spacecraft is used to keep the PM centered in its housing. This provides the best performance and simplifies the instrument by eliminating the electrostatic suspension force required to keep the PM centered along with its associated force noise. The Triad I and LISA Pathfinder missions have implemented true drag-free mode.

DRAG-FREE CUBESAT

Drag-free spacecraft utilizes a gravitational reference sensor (GRS) to shield an internal free-floating proof mass (PM) from both external disturbances and disturbances caused by the spacecraft (SC) itself.[11] The GRS measures the position of the spacecraft with respect to the PM and a feedback control system commands a propulsion system to keep the spacecraft centered about the PM. The key technologies are a) the GRS itself, consisting of a high density and homogenous PM shielded from all non-gravitational forces and a sensor to precisely measure the position of the spacecraft relative to the PM, b) a caging mechanism to prevent damage to the PM during launch and to release the PM upon arrival on orbit, and c) a

charge management system that keeps the PM and spacecraft electric potentials in equilibrium. In principle, the PM is then completely freed from non-gravitational disturbances so that it and its 'tender' spacecraft follow a pure geodesic.

Drag-free spacecraft design is a trade-off between system complexity, fuel conservation, cost of components, cost of operations, and performance.[1] In this section, a simple and cost-effective design for a drag-free nanosatellite for autonomous Earth observation and in-situ atmospheric studies is explored. The nanosatellite is composed of a single-thruster to compensate for drag and an attitude control system to orient the spacecraft in the direction of the dominant external disturbance force. The stability of the spacecraft and its ability to recover the external disturbance force vector is demonstrated on a flight-ready nanosatellite processor interfaced with a personal computer (PC) that models the spacecraft dynamics. It targets all applications discussed in Table 1 except gravitational wave detection, and achieves a modest acceleration noise performance of $<10^{-12}$ ms^{-2}Hz$^{-1/2}$ around 1 mHz.

As with most previous drag-free missions, the system simplicity is derived from the entire control system, which includes: the inertial sensor, thruster, attitude determination and control system (ADACS), and drag-free attitude and control system (DFACS); all considered as a single instrument. This new configuration utilizes a commercially available ADACS, which measures and controls the roll, pitch and yaw angles of the spacecraft, a GRS, which consists of a housing that contains and shields a free-floating spherical PM and provides measurements of the position of the spacecraft relative to the PM (Sun 2006); and a single thruster to compensate for drag. The position is measured by a differential optical shadow sensor (DOSS)[12] mounted to four sides of the housing. By utilizing a spherical PM, the need for PM attitude control (e.g. via an electrostatic suspension system) is eliminated since the sphere is orientation-invariant to a high degree.[8] We also assume a true drag-free configuration, which in several ways is simpler than an accelerometer mode drag-free system. This is because a true drag-free system does not use an inner-PM control loop, and therefore does not require the associated control logic and actuation system. Additionally, the advent of small and nanosatellites have provided a myriad of low-cost technologies that are important for drag-free operation. These include low-power computers and micro-processors, compact solid-state optical emitters and sensors, miniature and lower cost ADACS, and a variety of micro-propulsion systems. By taking advantage of these new technologies and

utilizing a small GRS with a single-thruster as a means to compensate for disturbance forces acting on a nanosatellite, fuel economy is optimized and therefore the mission lifetime is extended.

A twelve-degree of freedom simulation was performed to evaluate the performance of the drag-free CubeSat. The simulation block diagram is shown in Figure 1.
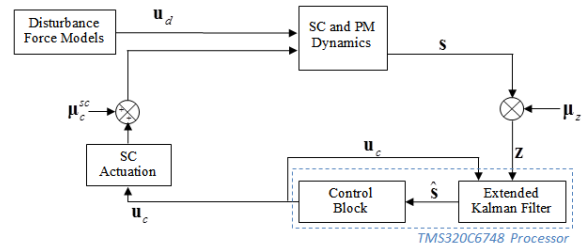

Figure 1: Simulation block diagram

Spacecraft

Because of their increasing ubiquity as secondary payloads, a nanosatellite in a CubeSat form factor is adopted for this simulation. A demonstration mission might be accommodated in a 3-unit (3U) (10 cm × 10 cm × 34 cm) CubeSat shown in Figure 2.[8] It is assumed to have solar panels on all sides and weigh 4 kg upon launch in a 400 km circular polar orbit with parameters listed in Table 1. Off-axis moments of inertia and propulsion mass loss are neglected in this simulation.
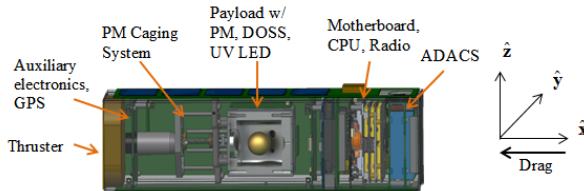

Figure 2: 3U CubeSat candidate[12]

The performance of the DFACS is governed by the minimum thrust bit applied by the single-thruster at the aft of the spacecraft. The $\hat{\mathbf{x}}$, $\hat{\mathbf{y}}$ and $\hat{\mathbf{z}}$ body-fixed axes are defined as shown in Figure 1, and it is assumed that the thruster can only apply a force in the $\hat{\mathbf{x}}$ direction.

A MEMS-based electric micro-thruster system is selected as the thruster for this simulation. It is a proportional device that utilizes electrostatic extraction and acceleration of positive and negative ions from an ionic liquid, to provide fine thrusting, and has

advantages over cold-gas thrusters in terms of mass, volume and simplicity of operation. Although this technology is relatively new and limited, it still can be commercially purchased through Busek Company, Inc (2016). Other groups developing this technology include Massachusetts Institute of Technology.[13] For the simulation that utilizes an electric micro-thruster, an impulse of 2 µN-s (min.), 80 µN-s (max.), and minimum sampling time of 5 ms with white noise of 2 µN (RMS).

The attitude of the SC is determined and controlled using a commercial ADACS that utilizes a combination of a horizon sensor and rate gyroscopes placed at the front-end of the spacecraft. Based on the specifications from a variety of suppliers such as Clyde Space, Maryland Aerospace Inc., and Blue Canyon Technologies, a maximum torque of 0.6 mN-m with pointing white noise of 0.014° (RMS) is assumed. Note that the spacecraft torque noise associated with the ADACS is included in the pointing noise. A summary of the spacecraft actuation and measurement noise parameters are given in Table 2.

Table 2: Spacecraft parameters

Parameter	Symbol	Value	Units
Orbit		Circular Polar	
Altitude	h	400	km
Period	T	5554	s
Mass	m_{sc}	4	kg
Length	l_{sc}	34	cm
Width	w_{sc}	10	cm
Height	h_{sc}	10	cm
Principal Moments of Inertia	$\underline{\underline{\mathbf{I}}}^{SC}$	$I_x = \frac{1}{12} m_{sc}\left(w_{sc}^2 + h_{sc}^2\right) = 0.0067$ $I_y = \frac{1}{12} m_{sc}\left(l_{sc}^2 + w_{sc}^2\right) = 0.0419$ $I_z = \frac{1}{12} m_{sc}\left(l_{sc}^2 + h_{sc}^2\right) = 0.0419$	kg m^2

Table 3: Spacecraft actuation and measurement noise parameters

Parameter		Source	Symbol	RMS	Units
Actuation	Position	Cold-gas thruster	μ_{Fcg}^{sc}	5	mN
		EP	$\mu_{F\ EP}^{sc}$	2	µN
Measure-ment	Position	GPS	μ_{r}^{sc}	10	m
	Orienta-tion	ADCS	μ_{q}^{sc}	0.014	deg

Gravitational Reference Sensor

The GRS is a high precision, compact, and inertial sensor developed by Stanford University.[12] The differential optical shadow Sensor (DOSS), utilizes four light-emitting diodes (LEDs) to measure the position of the PM relative to the housing and transmits this data to the DFACS to control the position and orientation of the outer spacecraft. The measured noise profile of a DOSS prototype is shown in Figure 3. In the simulations, a 10 nmHz$^{-1/2}$ (or 3.16 nm at 10 Hz) white measurement noise is assumed.
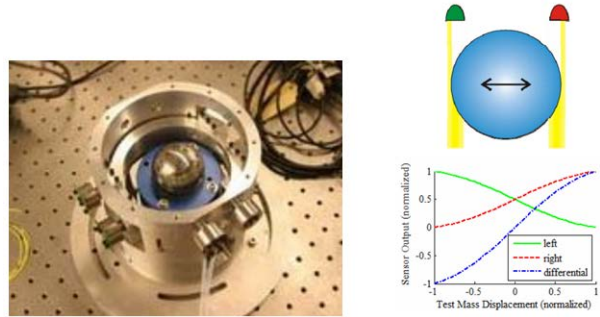

Figure 3: Differential optical shadow sensor[12]
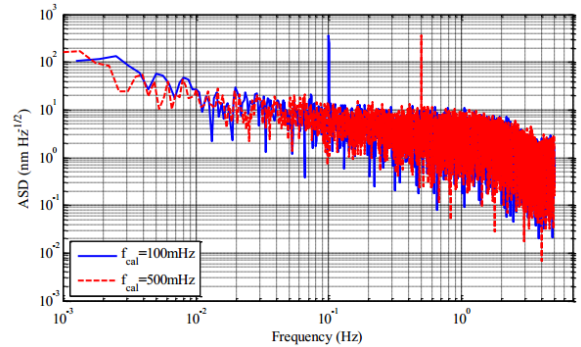

Figure 4: DOSS noise profile[12]

Environmental Disturbances

The total disturbance forces from atmospheric drag, solar radiation pressure, earth radiation pressure, stiffness and high frequency contributions acting on the candidate nanosatellite at a 400 km circular polar orbit are shown in Figure 5, over roughly 6 orbits. The high-frequency contributions are added to account for the complex random processes that govern the disturbance environment in Earth orbit at frequencies at above f = 1 mHz.
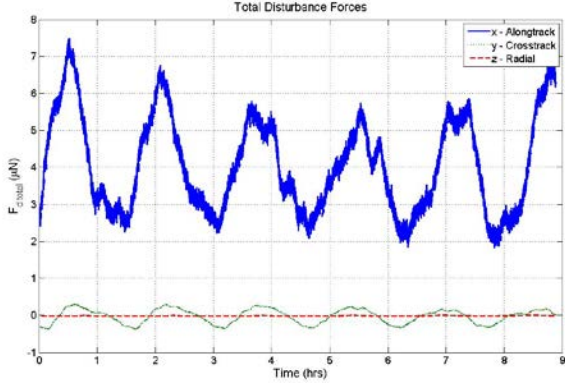
Figure 5: Total external disturbance forces on a 4 kg nanosatellite in 400 km circular polar orbit

The amplitude spectral density (ASD) of the high-frequency contributions from the external disturbance forces are shown in Figure 6. These disturbances are well below the maximum capability of the thruster, which is 80 µN, and the torque capability of the ADACS.
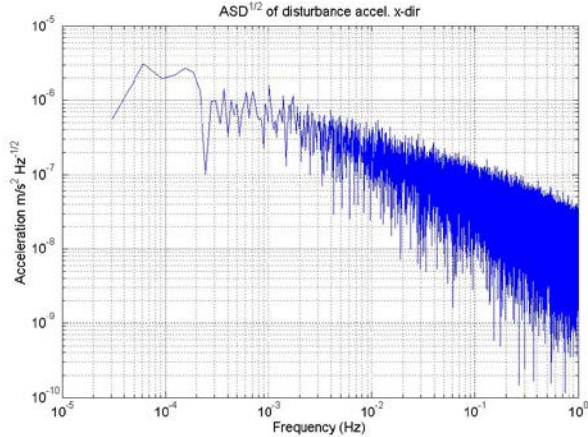

Figure 6: ASD of high frequency contribution of atmospheric drag, solar radiation pressure, and Earth radiation pressure accelerations along-track

Control System

The DFACS provides a 3-axis translation control and stabilization using only one thruster at the aft of the SC, making it the most fuel-efficient drag configuration since every impulse bit is used to directly compensate for the disturbance force. The drag-free attitude and control algorithm for the system consists of: a switching line or curve for the translational $\hat{\mathbf{x}}$ direction, a slower attitude control loop for the roll angle, ϕ, and a nested faster attitude control loop and a slower translational control loop for the transverse $\hat{\mathbf{y}}$ and $\hat{\mathbf{z}}$ directions with

associated pitch and yaw angles, θ and ψ, respectively.

The control law for the electric thruster follows a switching curve. In order to prevent chatter about the origin, a proportional control law is implemented in the linear range. A relatively slow linear attitude control law is used to control the roll angle. For the transverse directions and angles, a faster inner attitude control loop keeps the SC oriented in the direction of the main disturbance force and a slower outer translational control loop keeps the spacecraft positioned with respect to the PM. Here, the outer translational actuation is performed with the thruster, along with reaction wheels from the ADACS.

Figure 7 shows control block diagram for the transverse directions. The control gains of the outer- and inner-loop are K_{OL} and K_{IL}, while the plant dynamics transfer functions of the outer- and inner-loops are G_{OL} and G_{IL} are, respectively. The resulting forces from the single thruster transformed from the body $\hat{\mathbf{x}}$ to the quasi-inertial $\hat{\mathbf{I}}_y$ and $\hat{\mathbf{I}}_z$ directions are F_{cy} and F_{cz}. The commanded torques about the roll, pitch, and yaw angles are $T_{c\phi}, T_{c\theta}, T_{c\psi}$, while y and z are the displacements in the spacecraft body-fixed $\hat{\mathbf{y}}$ and $\hat{\mathbf{z}}$ directions, respectively.
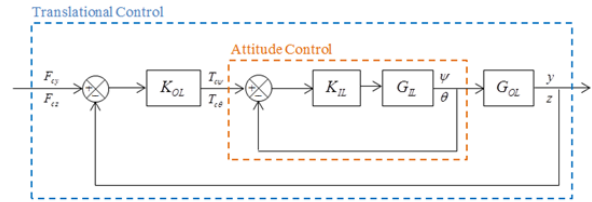

Figure 7: DFACS transverse control block diagram

External Disturbance Force Estimation

Using the position and orientation of the spacecraft measured by the DOSS and ADACS, the disturbance forces acting on the spacecraft are back-estimated. To do this, an 18-state EKF, along with standard estimation techniques as mentioned previously are used. First, the accelerations from the EKF are estimated, where the estimated acceleration errors are shown in Figure 8 and Table 4.
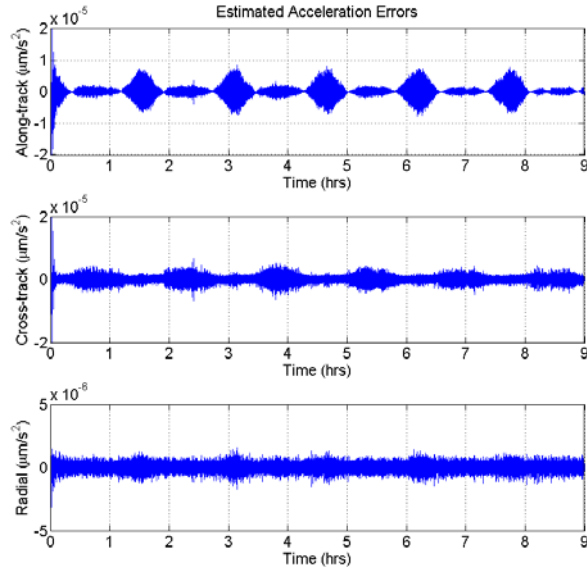
Figure 8: Estimated acceleration errors

Table 4: RMS of true and estimated acceleration errors

	RMS $\left(\mu ms^{-2}\right)$
$\Delta\ddot{x}$	1.2×10^{-6}
$\Delta\ddot{y}$	1.3×10^{-6}
$\Delta\ddot{z}$	9.1×10^{-7}

An a priori estimated bias and drift term are added to compensate for accelerometer bias and drift, and the external disturbance forces are estimated with a low-pass 10th order Butterworth filter with a normalized cut-off frequency of 1 Hz. The resulting true and estimated external disturbance errors are shown in Figure 9 and Table 5. Although optimal, the EKF does not estimate the states perfectly due to nonlinearities in the dynamics. This is due to the known estimation bias, which occurs using an EKF on certain types of nonlinear problems.[14] However, we can conclude that the estimated and true disturbance forces are a reasonable preliminary result, and further work may be done to better estimate the accelerometer bias and drift.
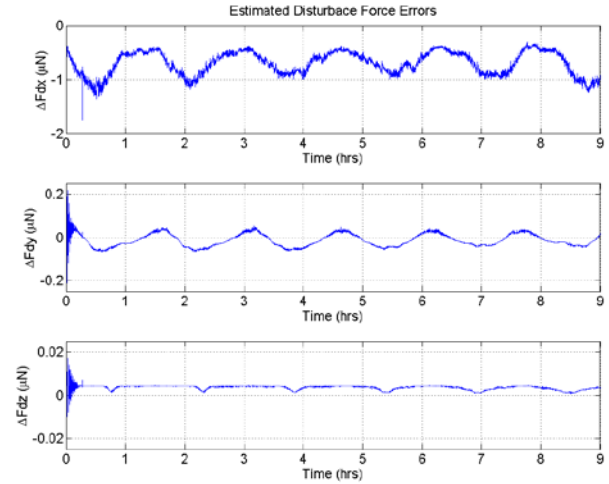

Figure 9: True and estimated external disturbance errors.

Table 5: RMS of true and estimated acceleration errors

	RMS $\left(\mu ms^{-2}\right)$
$\Delta\ddot{x}$	9.2×10^{-1}
$\Delta\ddot{y}$	4.7×10^{-3}
$\Delta\ddot{z}$	3.8×10^{-3}

Performance

The drag force recovery performance, which is the spacecraft acceleration measurement error, is the difference between the true and the measured spacecraft accelerations. The along-track amplitude spectral density (ASD) of the external disturbance measurement error can be seen in Figure 10. For the transverse directions, the residual external disturbance acceleration errors at 10 mHz are shown in Table 6. These results can be compared with the PM acceleration noise in Conklin[8], which is ~10^{-12} ms^{-2}Hz$^{-1/2}$. The external disturbance measurement error is limited by the amount of thruster noise. The RMS of the applied thrust force and ADACS torques are also shown in Table 6. The total performance of the system can be improved with a lower-noise thruster.
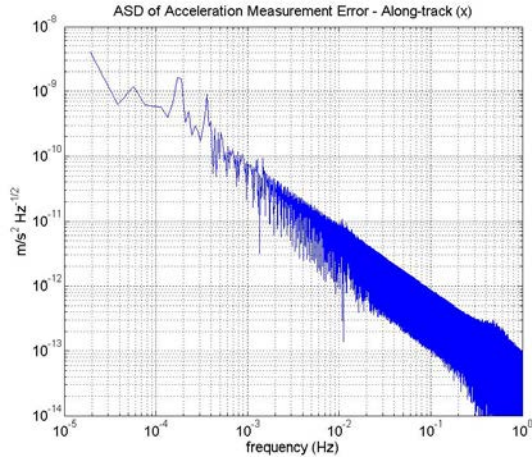
Figure 10: ASD of acceleration measurement error along-track

Table 6: Residual acceleration measurement error at 10 mHz and RMS of applied force and torque

Direct-ion	ASD $(ms^{-2}Hz^{-1/2})$	RMS of applied force (N)	RMS of applied Torque (N)
$\hat{x}$	10^{-11}	5.7×10^{-6}	6.2×10^{-5}
$\hat{y}$	10^{-11}	0.0	4.4×10^{-4}
$\hat{z}$	10^{-12}	0.0	5.2×10^{-4}

DRIFT-MODE ACCELEROMETER

As mentioned in the introductory section, there are two standard approaches to precise accelerometry measurements, via an electrostatic accelerometer (EA) or a drag-free system.

The first approach to precise acceleration measurements is via an electrostatic accelerometer (EA). An EA consists of an internal free-floating metallic proof mass (PM) surrounded by an electrode housing. The proof mass' position is capacitively measured via electrodes on the internal surface of the housing, which are also used to drive the electrostatic suspension system to keep the PM centered in the housing. The resulting internal acceleration of the spacecraft is proportional to the suspension force applied to the PM.

The most precise EAs are manufactured are produced by ONERA, which are capable of measuring spacecraft acceleration relative to the inertial frame to ~10^{-11} $ms^{-2}Hz^{-1/2}$ from about 1 mHz to 1 Hz.[6] To date, EAs have been used for Earth geodesy missions, including the 2000 CHAllenging Minisatellite Payload (CHAMP)[15], the 2002 Gravity Recovery and Climate

Experiment (GRACE)[2] and 2009 Gravity Field and Steady-State Ocean Circulation Explorer (GOCE)[16].

The accuracy of EA is limited by two inter-related factors: 1) suspension force noise, and 2) acceleration measurement noise. Both are ultimately related to the stability of voltage references, where the current state of the art is ~ 2×10^{-6} V/(V Hz$^{1/2}$).[17] Depending on the altitude, mass, and cross-sectional area of a low Earth orbiting spacecraft, the nominal acceleration can be on the order of 10^{-5} ms^{-2}. Therefore, the resulting acceleration on the PM due to the suspension system can be ~2×10^{-11} ms^{-2}. Since the applied suspension force is the acceleration measurement, the acceleration measurement noise is on the same order. To improve the accelerometers beyond the 10^{-11} ms^{-2} level, the stability of voltage references must be greatly improved or the suspension force noise must be removed all together.

The second approach to precise acceleration measurements is a drag-free system. Drag-free technology is the most promising approach to breaking through the acceleration noise limits. First conceived in the 1960's, drag-free spacecraft utilizes a gravitational reference sensor (GRS) to shield an internal free-floating PM from both external disturbances and disturbances caused by the spacecraft (SC) itself.[18] The GRS measures the position of the spacecraft with respect to the PM and a feedback control system commands a propulsion system to keep the SC centered about the PM. The key technologies are 1) the GRS itself, consisting of a high density and homogenous PM shielded from all non-gravitational forces and a sensor to precisely measure the position of the SC relative to the PM, 2) a caging mechanism to prevent damage to the PM during launch and to release the PM upon arrival on orbit, and 3) a charge management system that keeps the PM and SC electric potentials in equilibrium.

The new approach discussed in this section is a drift-mode accelerometer (DMA), which is an off-shoot of the drift-mode operation used for the LPF mission. The LPF contains two free-floating proof masses and aims to demonstrate a differential acceleration noise between two proof masses below 10^{-14} $ms^{-2}Hz^{-1/2}$ over a frequency band of 1–3 mHz. LPF estimates the PM acceleration noise contributions from a myriad of sources, including noise caused by its electrostatic suspension system. Since the SC can only fly drag-free about one PM, the other PM must be suspended against the external disturbance forces. In order to assess the acceleration noise contribution from this suspension system force, the drift-mode operation was conceived. The LPF drift-mode will operate on a very low duty

cycle, 200 s between 1 s impulses. In between impulses, the PM follows parabolic trajectories when measured relative to the drag-free PM. A laser interferometer is used to measure the differential displacement of the two PMs to high precision, and the resulting measurement is fit to a second order polynomial. The fit residuals are used to calculate variations in the differential acceleration between the two PMs. The laser interferometer data is replaced with a model of the acceleration noise that makes various assumptions about the nature and stationary of the noise.[19]

The DMA is a new class of inertial sensor that is a hybrid electrostatic accelerometer/drag-free system. This system consists of 1) an electrostatic accelerometer and 2) a laser interferometer. Unlike a typical EA, where the suspension system is always on, a DMA cycles the suspension system to suppress the contributions of the suspension force noise over known periodic intervals, similar to drift-mode control for LPF. However, the DMA operates on a low duty cycle, 5 s in between 1 s impulses, above the science frequencies of interest. The DMA PM is considered drag-free between impulses, resulting in an acceleration noise comparable to a drag-free system, without the need for an external propulsion system for the SC. The electrostatic suspension noise, suspension force as a readout of the SC acceleration, and the resulting science measurements are no longer limited to the dynamic range of the capacitive readouts from the electrostatic accelerometer through use of the laser interferometer. Although the operations are similar, the drift-mode operation for LPF is mainly intended for a drag-free SC and the drift-mode control for a DMA is intended for non-drag-free SC.[20]

A completely numerical 12 degrees-of-freedom simulation (6 for the SC and 6 for the PM) to evaluate the dynamics, control and performance of such a device, shown in Figure 11.
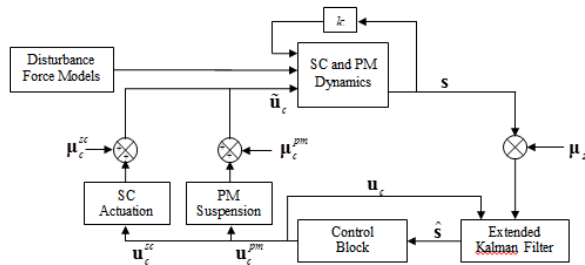

Figure 11: DMA simulation block diagram

Spacecraft

The candidate spacecraft for a DMA is one similar to that of a small satellite proposal for GRACE-II (Sheard 2012). GRACE-II intends to extend and improve on the first GRACE mission by replacing the microwave ranging system with a laser-based satellite-to-satellite interferometer and operate drag-free. This spacecraft is an ideal candidate for the DMA since the proposed mission contains all of the components required for a drift-mode operation.
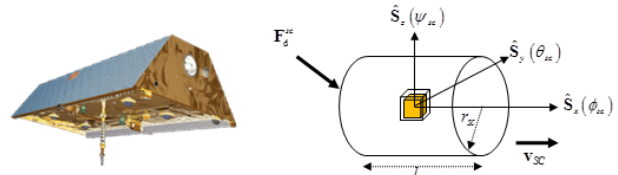

Figure 12: GRACE Follow-on and the simplified version of SC modeled

Table 7: Spacecraft parameters

Parameter	Symbol	Value	Units
Orbit		Circular Polar	
Altitude	h	400	km
Period	T	5554	s
Mass	m_{sc}	250	kg
Cylinder Radius	r_{sc}	0.7	m
Cylinder Length	l_{sc}	10	m
Principal Moments of Inertia	$\underline{\mathbf{I}}^{SC}$	$I_x = \frac{1}{2}m_{sc}r_{sc}^2 = 61.25$ $I_y = I_z = \frac{1}{2}m_{sc}r_{sc}^2 + \frac{1}{12}m_{sc}l_{sc}^2$ $= 102.08$	kg m²

Similar to the drag-free CubeSat, the SC is assumed to have global positioning system (GPS) to measure the position of the SC, with white noise of 10 m sampled at 10 Hz. The SC attitude is determined by combination of a horizon sensor and rate gyroscopes placed at the front-end of the SC. Based on the specifications from a variety of suppliers such as Clyde Space, Maryland Aerospace Inc., and Blue Canyon Technologies, a maximum torque of $\tau_{MAX}^{pm} = 0.6$ Nm with pointing white noise of 0.014° (RMS) is assumed.[21,22,23] Note that the SC torque noise associated with the ADACS is included in the pointing noise. Additionally, the SC actuation force noise is not included in the simulation, since both electrostatic accelerometer and drift-mode accelerometer do not require any spacecraft actuation (e.g. via a propulsion system).

GRS

The drift-mode accelerometer consists of free-floating, high-density cubic proof mass, surrounded by an outer housing rigidly attached to the SC. The housing contains electrodes that 1) electrostatically actuates the PM and 2) capacitively measures the PM displacement and orientation. A laser interferometer provides a precision readout of the PM displacement x, in the sensitive direction, $\hat{\mathbf{S}}_x$. The CMs and body-fixed axes of the PM and SC are initially co-aligned along $\hat{\mathbf{x}}, \hat{\mathbf{y}}, \hat{\mathbf{z}}$ and $\hat{\mathbf{S}}_x, \hat{\mathbf{S}}_y, \hat{\mathbf{S}}_z$, respectively, shown in Figure 13.

Figure 13: PM geometry and cross-sectional view

The roll, pitch, and yaw angles of the PM, $\phi_{pm}, \theta_{pm}, \psi_{pm}$ are about its $\hat{\mathbf{x}}, \hat{\mathbf{y}}, \hat{\mathbf{z}}$ axis, respectively. The length of the PM is a_{pm}, with housing-PM gap distance d. For a drift-mode accelerometer, the gap is chosen to be relatively small (d = 1 mm), because a relatively large suspension force is needed to support the PM against atmospheric drag in low Earth orbit. The simulation values of the described proof mass parameters are listed in Table 8.

Table 8: Proof mass parameters

Parameter	Symbol	Value	Units
Mass	m_{pm}	0.24	Kg
Cubic Length	a_{pm}	3	Cm
PM-Housing Gap	D	1	Mm
Principal Moment of Inertia	$\underline{\underline{\mathbf{I}}}^{pm}$	$\begin{bmatrix} I_x & 0 & 0 \\ 0 & I_y & 0 \\ 0 & 0 & I_z \end{bmatrix}$ $I_x = I_y = I_z = \frac{1}{6} m_{pm} a_{pm}^2$	kg m^2

The PM electrostatic suspension system (ESS) is assumed to have a force noise of $\mu_F^{pm} = F_{MAX}^{pm} \cdot 2 \times 10^{-6}$ NHz$^{-1/2}$, modeled as white noise, where the maximum force the ESS can apply is F_{MAX}^{pm} = 50 µN. The associated white torque noise is simplified

as $\mu_\tau^{pm} = \operatorname{atan2}\left[F_{MAX}^{pm} \big/ \left(0.5 \cdot a_{pm}\right)\right]$, where $\tau_{MAX}^{pm} =$ 3.3×10^{-3} Nm. The capacitive sensors of the ESS are assumed to have a white measurement noise of 1.0×10^{-8} m and associated orientation measurement noise of 3.8×10^{-9} rad as measured in Racca[10] and Chilton[24]. For the sensitive direction, the laser interferometer is assumed to have a white noise of 1×10^{-12} m and associated orientation measurement noise of 3.8×10^{-9} rad.[20]

Spacecraft Disturbances

The total disturbance forces from atmospheric drag, solar radiation pressure, earth radiation pressure, stiffness and high frequency contributions acting on a GRACE-II-like spacecraft in a 400 km circular polar orbit are shown in Figure 14 over roughly 6 orbits. Again, the high-frequency contributions are added to account for the complex random processes that govern the disturbance environment in Earth orbit at frequencies at above f = 1 mHz and the ASD of the high-frequency contributions from the external disturbance forces are shown in Figure 15.
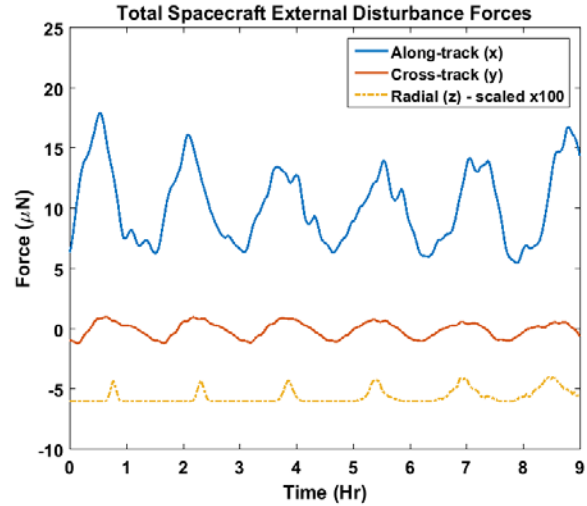

Figure 14: Total external disturbance forces on a 250 kg GRACE-II-like spacecraft in 400 km circular polar orbit.
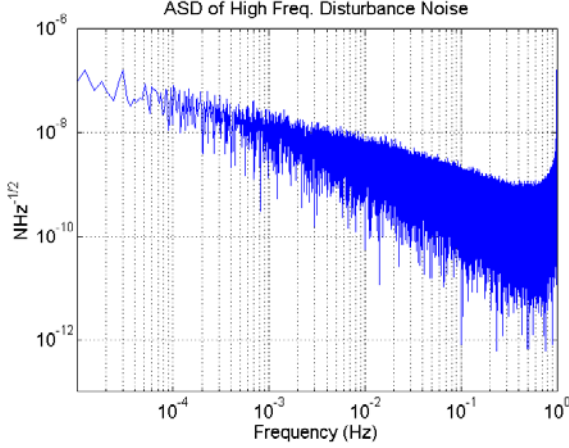
Figure 15: ASD of high frequency contribution of atmospheric drag, solar radiation pressure, and Earth radiation pressure accelerations along-track

Proof-mass Disturbance Noise Forces

The ASD of the PM acceleration noise contributions are shown in Figure 16 for the DMA and Figure 17 for the EA. The stiffness term F_k, is the residual coupling of SC motion to PM motion. The stiffness constant used in both modes is $k = 2.0$ $10{-}6$ N/m.[20] The difference between the magnitudes of the stiffness forces are due to the difference in PM displacement ultimately caused by the different control modes which are outlined in the Results section. It can be noted that the stiffness force magnitudes in the sensitive $\hat{\mathbf{x}}$ direction are about 10 times higher in DMA mode and 4 times higher in EA mode, than those in the $\hat{\mathbf{y}}$ and $\hat{\mathbf{z}}$ directions. This is due to the dominant external disturbance forces on the spacecraft acting in the along-track direction, which consequently cause the largest PM displacement along the same direction. The differential gravitational force F_g, is the difference between the gravitational pull on the SC from the Earth and the gravitational pull on the PM from the Earth. The force noise due to gap-dependent and gap-independent forces that do not depend on the relative dynamics of the PM and SC is denoted as F_a. This acceleration noise is comprised of a myriad of forces including surface forces which both depend and do not depend on gap-size. The overall disturbance force acting on the PM F_d, is dominated by the stiffness force. The apparent peaks shown in Figure 16 at 0.1 Hz and its harmonics are due to the DMA cycling. The apparent peak shown in Figure 17 at 0.4 Hz is due to the natural frequency of the lead-lag controller used in the control block. For the acceleration noise models used in this simulation, refer to Conklin[20].
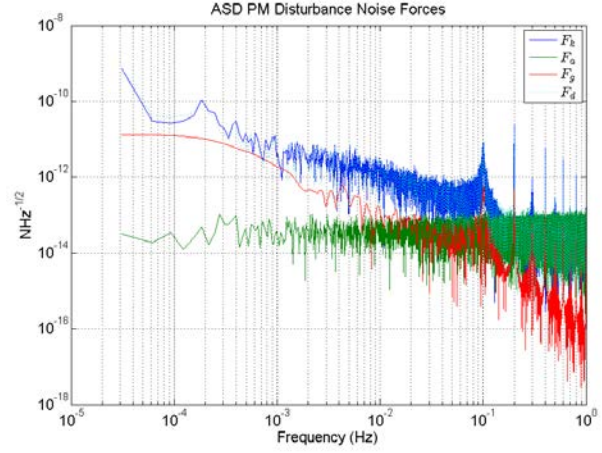

Figure 16: ASD of the PM acceleration noise contributions in DMA.
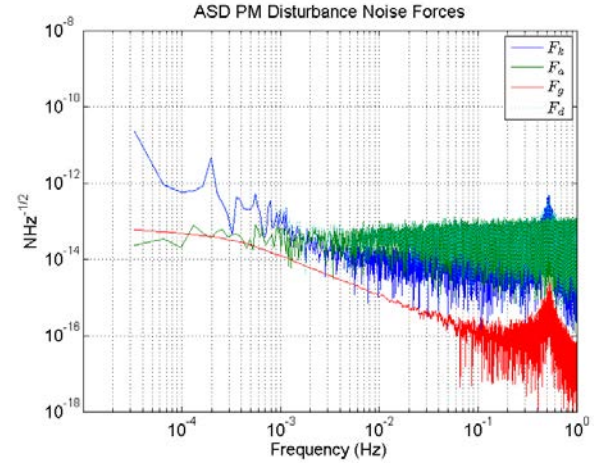

Figure 17: ASD of the PM acceleration noise contributions in EA.

Proof mass measurement noise forces

The PM measurement cross-coupling noise values outlined in Conklin[20] are given in Table 9. Since the measurement cross-coupling noise is dependent on the PM displacement and orientation, the values are denoted $\boldsymbol{\mu}_{cc-DMA}^{pm}$ for a DMA, and $\boldsymbol{\mu}_{cc-EA}^{pm}$ for an EA. Again, the measurement cross coupling values for an EA are roughly one order of magnitude lower than those of a DMA since the displacements of the PM due to drift-mode control are overall larger.

Table 9: PM measurement cross-coupling noise in m RMS

	$\boldsymbol{\mu}_{cc-DMA}^{pm}$	$\boldsymbol{\mu}_{cc-EA}^{pm}$
$\Delta\ddot{x}$	6.82×10^{-7}	2.41×10^{-8}

$\Delta\ddot{y}$	6.07×10^{-8}	6.88×10^{-9}
$\Delta\ddot{z}$	9.25×10^{-8}	6.72×10^{-9}

Drift-mode Control

A drift-mode accelerometer operates as a traditional electrostatic accelerometer with a suspension force that is cycled on and off. The suspension force noise is limited to brief and known time intervals that can be removed from the overall data. In theory, this system is able to achieve the performance of a drag-free system with the simplicity of an EA.

The equations of motion for the PM are simplified into 6 one-axis discretized lead-lag control equations. The continuous transfer function is converted to a discrete transfer function using a Tustin approximation and a zero-order hold on the input. The discrete transfer function is then written as an equivalent difference equation, shown in the control block diagram with drift-mode control logic in Figure 18. The drift-mode counter keeps track of the current time, desired drift-mode interval, and duty cycle. When the counter commands the suspension system off, the applied forces and torques to the PM are set to zero. When the counter commands the suspension on, the appropriate lead-lag controller is applied to the electrostatic suspension system. The commanded control forces and torques applied to the PM are $\mathbf{F}_{c[k]}^{pm}$ and $\boldsymbol{\tau}_{c[k]}^{pm}$. The commanded control force and torques at the previous time-step are $\mathbf{F}_{c[k-1]}^{pm}$ and $\boldsymbol{\tau}_{c[k-1]}^{pm}$. The estimated position of the PM relative to the SC-fixed reference frame at the current and previous time-step calculated by the EKF are $\mathbf{r}_{[k]}^{pm}$ and $\mathbf{r}_{[k-1]}^{pm}$ $\boldsymbol{\tau}_{c[k-1]}^{pm}$. The control gain vectors are $\mathbf{K}_{Fc}$ and $\mathbf{K}_{\tau c}$, the proportional gain vectors are $\mathbf{K}_{Fp}$ and $\mathbf{K}_{\tau p}$, and the derivative gain vectors are $\mathbf{K}_{Fd}$ and $\mathbf{K}_{\tau d}$.
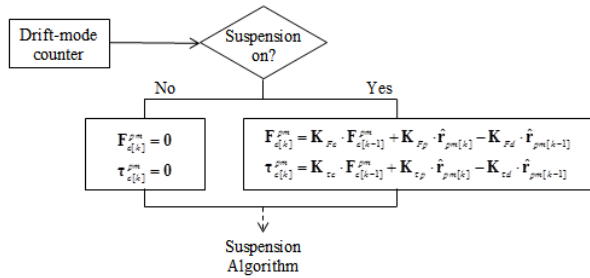

Figure 18: Drift-mode control logic block diagram.

In this simulation, the drift-mode interval is set to 5 s intervals with 10% duty cycle (e.g. 4.5 s off, 0.5 s on). The drift-mode control and resulting PM displacement arcs are shown in Figure 19. The shaded areas show the 0.5 s time intervals in which the suspension system is on and where the PM displacement read-outs would be removed from the overall data.
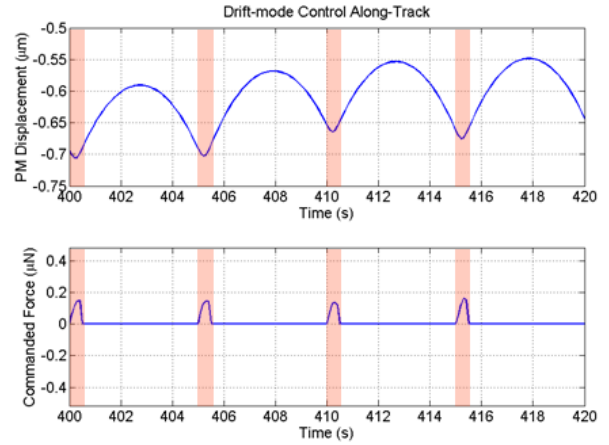

Figure 19: Drift-mode control and PM displacement.

Electrostatic Accelerometer Performance

The acceleration error of an electrostatic accelerometer serves as a basis for comparison for the performance of a drift-mode accelerometer. In this subsection, the acceleration error is calculated using the 0.1 Hz 10th order Butterworth-filtered PM displacement and electrostatic control force is shown in Figure 20. The control force is directly proportional to the disturbance force acting on the SC.
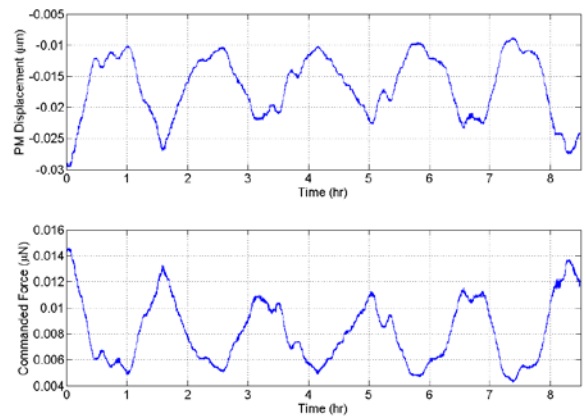

Figure 20: 100 Hz Butterworth-filtered PM motion and force for the EA

The amplitude spectral density (ASD) of the true acceleration and acceleration estimate error are shown in Figure 21. In the legend of this figure, the ASD of

the true disturbance acceleration is denoted as , the acceleration estimate error is denoted as , and the PM acceleration noise due to stiffness, gravitational potential, gap-dependent and gap-independent forces, and actuation cross-coupling are F_k, F_g, F_a, and F_{cc} respectively. The peaks at 0.4 Hz correspond to the zeros and poles selected from the lead-lag controller. As expected from Conklin[20], the limiting acceleration noise is roughly equal to the capacitive actuation noise and the actuation cross-coupling. The acceleration estimate error for the electrostatic accelerometer at 10^{-2} Hz is approximately 1.0×10^{-10} ms^{-2}Hz$^{-1/2}$.
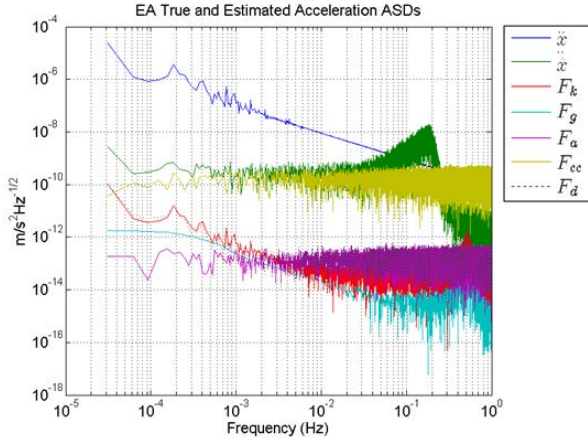

Figure 21: ASD of the true acceleration and the acceleration estimate error for an EA.

Drift-mode Accelerometer Performance

For a DMA, the SC acceleration information is contained in the laser interferometer output between the actuation impulses. The measured acceleration is estimated by fitting the PM displacement measurements to parabolic arcs, given in the equation below. The least-squares fit parameters are the position and velocity at $t = t_0$, x_0 and v_0, and the estimated mean acceleration is a_0.

$$x_{pm}^{meas} = x_0 + v_0\left(t - t_0\right) + \frac{1}{2}a_0\left(t - t_0\right)^2 \quad (2)$$

This approach, which has the advantage of being linear and uses all of the measured data, provides one acceleration measurement per drift interval. The resulting acceleration measurement noise (standard deviation), σ_a, depends linearly on the interferometer noise level n_{r-i}^{pm}, quadratically on inverse of the suspension cycling frequency, and inversely on the square root of the number of samples, N. With a 10 Hz

sampling frequency and duty cycle of 0.1, the number of samples, N, is roughly proportional to the interval time, T_{kick}. The estimated acceleration noise is given in the equation below[20], where α is an order of 1 and depends on the cross correlation between the mean acceleration and the constant and linear terms x_0 and v_0.

$$\sigma_a = \alpha \frac{\mu_{r-i}^{pm}}{T_{kick}^{5/2}} \quad (1)$$

The PM displacement and drift-mode control force is shown in Figure 22. Here, it is obvious that the control force is directly proportional to the disturbance force acting on the SC. The shorter term oscillations in the PM displacement are the parabolic arcs caused by the drift-mode control. As expected from Conklin[20] the limiting acceleration noise is due to the laser interferometer noise level and stiffness force.
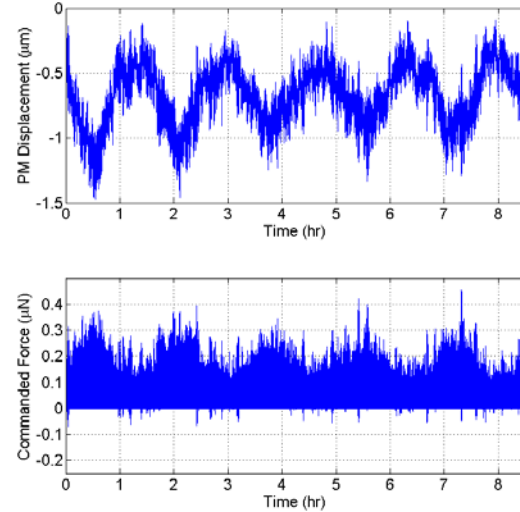

Figure 22: PM motion (top) and control force (bottom) for a DMA

The ASD of the true acceleration and acceleration estimate error for an uncompensated drift-mode accelerometer is shown in Figure 23. In the legend of this figure, the ASD of the true disturbance acceleration is denoted as $\ddot{x}$, the acceleration estimate error is denoted as $\hat{\ddot{x}}$, and the PM acceleration noise due to stiffness, gravitational potential, gap-dependent and gap-independent forces are F_k, F_g, and F_a respectively. The peaks at 0.2 Hz and its harmonics correspond to the 5 s time interval. The acceleration estimate error for a drift-mode accelerometer at 10^{-2} Hz is approximately 5.6×10^{-12} ms^{-2}Hz^{-2}.
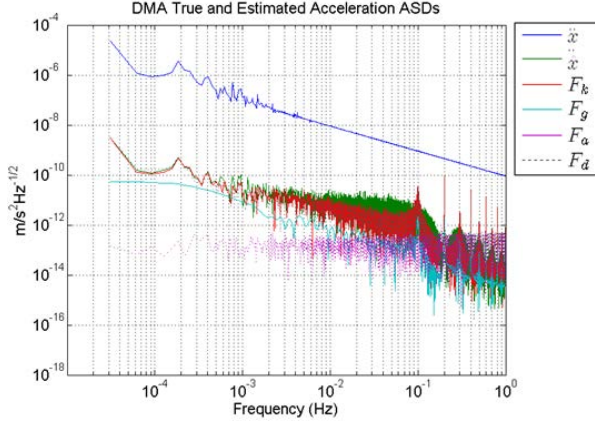
Figure 23: ASD of the true acceleration and the acceleration estimate error for a DMA

Use Letter or A4 size paper, with the margins set as indicated in Table 1. This template is set up for Letter size paper.

Compensated Drift-mode Accelerometer

The stiffness, differential gravitational potential, and measurement cross-coupling terms can be estimated and removed from the acceleration estimate. The differential gravitational potential and measurement cross-coupling terms can be directly estimated and removed from the acceleration estimate by using the EKF states. The stiffness term can be estimated via a calibration phase that varies the operational point of the drift-mode accelerometer by a known off-set. The estimated SC acceleration, $\ddot{\hat{x}}_{sc}$, is curve fit to the following equation:

$$\ddot{\hat{x}}_{sc} = \underbrace{k \cdot x_{pm}}_{\hat{F}_k} + \underbrace{\frac{GM_\oplus}{\left|\mathbf{r}_{pm/\oplus}\right|^3} x_{pm}}_{\hat{F}_g} + \underbrace{\sum_{i=1}^{8} A_i \cos\left(\frac{2\pi t}{T}\right) + B_i \sin\left(\frac{2\pi t}{T}\right)}_{\hat{F}_d} \quad (3)$$

where, the SC disturbance force is equal to the sum of the stiffness, differential gravitation, and external disturbance force $\hat{F}_k$, $\hat{F}_g$, and $\hat{F}_d$ respectively. The stiffness force in the $\hat{\mathbf{x}}$ direction is a function of the stiffness constant, k, and laser interferometer measured displacement of the PM, x_{pm}. The differential gravitational potential force in the in the $\hat{\mathbf{x}}$ direction is a function of the gravitational constant, $GM_\oplus$, known position of the PM with respect to the CM of the Earth (via GPS and capacitive sensors), $\mathbf{r}_{pm/\oplus}$, and position of the PM as measured by the laser

interferometer, x_{pm}. The unknown external disturbance force acting on the SC is modeled as a Fourier series of order 8 with the known spacecraft orbit period, T. The gap dependent and gap-independent forces are neglected from the estimation above since they are orders of magnitude smaller than the stiffness and differential gravitation force.

An example of a calibration phase with an 800 µm offset is shown in Figure 24. By elevating the stiffness related acceleration above the background noise level, k can be determined by fitting the linear model, $F_k^{pm} = k \cdot x_{pm}^{meas}$, to the interferometer data. Amplifying the stiffness results in a better estimation of k, but cannot be arbitrarily increased without fear of the PM hitting the housing wall.
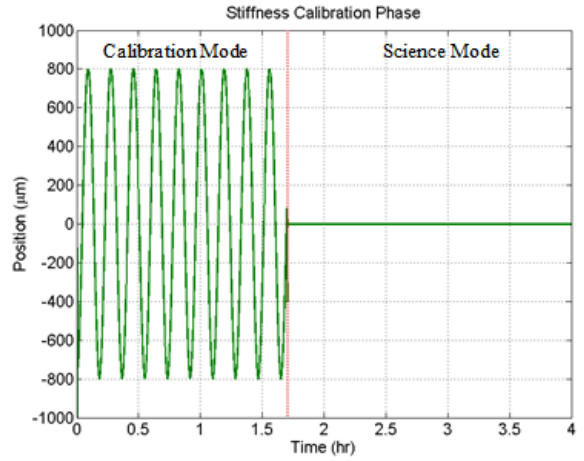

Figure 24: Stiffness calibration phase

The amplitude spectral density (ASD) of the estimated acceleration error for the compensated drift-mode accelerometer is shown in Figure 24. In the legend of this figure, the ASD of the true disturbance acceleration is denoted as $\ddot{x}$, the acceleration estimate error is denoted as $\ddot{\hat{x}}$, and the PM acceleration noise due to stiffness, gravitational potential, gap-dependent and gap-independent forces are F_k, F_g, and F_a respectively. As expected the acceleration noise is limited to the laser interferometer noise level. The peaks at 0.2 Hz and its harmonics correspond to the 5 s time interval. The residual accelerations for the electrostatic accelerometer (EA), drift-mode accelerometer (DMA) and compensated drift-mode accelerometer (c-DMA) are given in Table 9. The compensated drift-mode accelerometer gives the smallest estimated acceleration error compared to the

two other modes, as expected. The estimated acceleration error for a compensated drift-mode accelerometer at 10^{-2} Hz is approximately ~4.3×10^{-12} ms^{-2}Hz$^{-1/2}$.
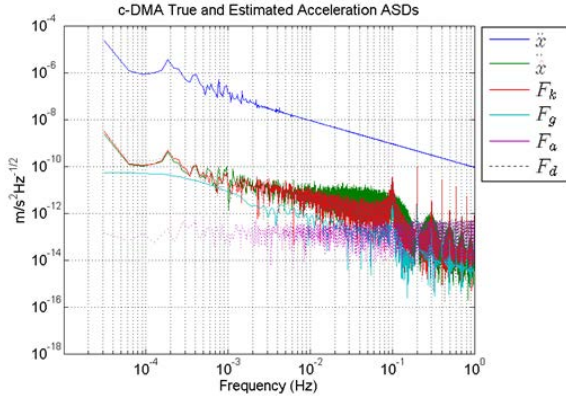

Figure 25: ASD of the true acceleration and the acceleration estimate error for a c-DMA.

When removing the laser interferometer noise from the simulation, it turns out that the estimation of the PM acceleration from parabolic trajectory is the next limiting factor with estimated acceleration error of 4.1×10^{-12} ms^{-2}Hz^{-2} at 10^{-2} Hz. To improve upon this result, a better technique may be used to estimate the PM acceleration from the parabolic curve trajectories.

Table 10: Estimated Acceleration Errors in $\hat{\mathbf{x}}$ - direction

Mode	ms^{-2}Hz$^{-1/2}$ at 10^{-2} Hz
EA	1.1×10^{-10}
DMA	5.6×10^{-12}
c-DMA	4.3×10^{-12}

FUTURE WORK

As the next major step in the development and characterization of the drift-mode accelerometer, a demonstration of the drift-mode control on flight-like hardware using the UF torsion pendulum is proposed. The experiment consists of running three different modes on torsion pendulum: 1) 'true' drag-free mode, 2) electrostatic accelerometer mode, and 3) drift-mode. The 'true' drag-free mode measurements are made on the UF torsion pendulum via a laser interferometer and with no applied external disturbance forces. The 'true' drag-free acceleration noise is measured to be ~10^{-12} ms^{-2}Hz$^{-1/2}$ at 10 Hz. The electrostatic accelerometer measurements are to be made via capacitive sensors, with a constant applied external disturbance force, and

electrostatic suspension system always on. The electrostatic accelerometer acceleration noise is directly proportional to the known applied control forces on the PM and limited to the capacitive actuation noise on the system. The drift-mode accelerometer measurements are to be made via a laser interferometer, with constant applied external disturbance force, and electrostatic suspension system on a low duty cycle. The drift-mode acceleration noise should be estimated from the parabolic arc motion of the PM during the intervals when the suspension system is completely off. The drift-mode acceleration noise should be on the same order of magnitude as the 'true' drag-free acceleration noise measurement. This demonstration would prove that a DMA can provide acceleration measurements with a noise performance similar to that of drag-free systems.

Ultimately, the best way to test two technologies presented in this dissertation is to demonstrate the technologies in space.

CONCLUSION

This paper explores two different types of drag-free spacecraft. Each system is analyzed with a complete 12 degree-of-freedom numerical simulation at a 400 km circular polar orbit is modeled followed with an analysis of the drag-free performance and drag-force recovery.

The first simulation is a drag-free nanosatellite with three-axis drag-free control utilizing a single axis MEMS based electric micro-thruster propulsion. Disturbance forces are empirically modeled, and an EKF along with a drag-free attitude and control system is developed to optimally estimate the position, velocity, angular displacement, and angular velocity of the satellite relative to the proof mass. The control algorithms are successfully implemented on a space-capable microprocessor, realistically demonstrating the stability of the entire system and its ability to keep the PM centered within the housing at 50 times per second. Disturbance force recovery to the level of 1 μN, 10^{-1} μN, and 10^{-2} μN in the spacecraft body-fixed $\hat{\mathbf{x}}$, $\hat{\mathbf{y}}$, and $\hat{\mathbf{z}}$ directions, respectively, is also demonstrated using the measured satellite displacement, attitude, and the applied thrust. The next steps for the single-thruster nanosatellite are to apply an alternate optimal estimator to eliminate the bias in the estimated disturbance forces from the extended Kalman filter and apply a full SC inertia dyadic to the simulation. Additionally, the performance can also be improved by reducing the propulsion noise with improved electric propulsion system.

The second simulation is that of a drift-mode accelerometer (DMA), which is a hybrid electrostatic accelerometer (EA)/drag-free system. A DMA incorporates an electrostatic accelerometer with the suspension system operated with a low, known duty cycle. The readout of the PM displacement is performed with a laser interferometer, which exceeds the limitations of traditional electrostatic accelerometer capacitive readouts. The data during the intervals when the suspension system is on is disregarded from the overall data analysis so that all acceleration noise due to the suspension system is eliminated. By estimating the stiffness and measuring cross-coupling terms, the DMA is limited only to the read-out noise of the laser interferometer, achieving a drag-free performance without the need for a complex propulsion system like that of true drag-free systems. An EA is first simulated to provide a baseline measurement with an acceleration noise on the order of 10^{-10} ms^{-2}Hz$^{-1/2}$ at 10^{-2} Hz, limited by the electrostatic actuation noise. It is shown that a DMA is able to achieve an acceleration noise on the order of 10^{-12} ms^{-2} Hz$^{-1/2}$ at 10^{-2} Hz, as expected from the theoretical calculations. It is then shown that a compensated DMA (c-DMA), can improve the DMA measurement by estimating the stiffness and differential gravitational potential disturbance acceleration terms. Overall improvements can be made to the drift-mode control by replacing the discretized lead-lag controller with a more optimal or nonlinear controller to reduce the apparent peaks from the natural frequency of the system. Better acceleration estimation techniques might be used to improve the curve-fitting of the parabolic proof mass motion from the drift-mode can also be explored, along with effects of higher order stiffness and stiffness estimation techniques.

ACKNOWLEDGMENTS

References

1. Leitner, J. (2003). Investigation of drag-free control technology for earth science constellation missions. Final Study Report to NASA Earth Science Technology Office, 15.

2. Tapley, B. D., Bettadpur, S., Watkins, M., & Reigber, C. (2004). The gravity recovery and climate experiment: Mission overview and early results.Geophysical Research Letters, 31(9).

3. Everitt, C. F., DeBra, D. B., Parkinson, B. W., Turneaure, J. P., Conklin, J. W., Heifetz, M. I., & Al-Meshari, M. (2011). Gravity probe B: final results of a space experiment to test general relativity. Physical Review Letters, 106(22), 221101.

4. Bertolami, O., Páramos, J., & Turyshev, S. G. (2008). General Theory of Relativity: Will it survive the next decade? (pp. 27-74). Springer Berlin Heidelberg.

5. The Space Department, S.O., The Guidance, S.O., & Laboratory, C. (1974). A Satellite Freed of all but Gravitational Forces:" TRIAD I". Journal of Spacecraft and Rockets, 11(9), 637-644.

6. Touboul, P., Rodrigues, M., Métris, G., & Tatry, B. (2001). MICROSCOPE, testing the equivalence principle in space. Comptes Rendus de l'Académie des Sciences-Series IV-Physics, 2(9), 1271-1286.

7. Benkhoff, J., van Casteren, J., Hayakawa, H., Fujimoto, M., Laakso, H., Novara, M., & Ziethe, R. (2010). BepiColombo—Comprehensive exploration of Mercury: Mission overview and science goals. Planetary and Space Science, 58(1), 2-20.

8. Conklin, J. W., & Gravity Probe B Collaboration. (2008). The Gravity Probe B experiment and early results. In Journal of Physics: Conference Series (Vol. 140, No. 1, p. 012001). IOP Publishing.

9. Canuto, E. (2008). Drag-free and attitude control for the GOCE satellite. Automatica, 44(7), 1766-1780.

10. Racca, G. D., & McNamara, P. W. (2010). The LISA pathfinder mission. Space science reviews, 151(1-3), 159-181.

11. DeBra, D. B. (1997). Drag-free spacecraft as platforms for space missions and fundamental physics. Classical and Quantum Gravity, 14(6), 1549.

12. Zoellner, A., Hultgren, E., & Sun, K. X. (2013). Integrated differential optical shadow sensor for Modular Gravitational Reference Sensor. arXiv preprint arXiv:1302.1623

13. Lozano, P., & Courtney, D. (2010). On the development of high specific impulse electric propulsion thrusters for small satellites. Madeira, Portugal, June.

14. Welch, G., & Bishop, G. (2006). An introduction to the Kalman filter. Department of Computer Science, University of North Carolina.

15. Reigber, C., Schwintzer, P., Neumayer, K. H., Barthelmes, F., König, R., Förste, C., & Bruinsma, S. (2003). The CHAMP-only Earth gravity field model EIGEN-2. Advances in Space Research, 31(8), 1883-1888.

16. Drinkwater, M. R., Floberghagen, R., Haagmans, R., Muzi, D., & Popescu, A. (2003). GOCE: ESA's first Earth Explorer Core mission. In Earth gravity field from space—From sensors to earth sciences (pp. 419-432). Springer Netherlands.

17. Christophe, B., Marque, J., & Foulon, B. (2010, December). In-orbit data verification of the accelerometers of the ESA GOCE mission. In SF2A-2010: Proceedings of the Annual meeting of the French Society of Astronomy and Astrophysics (Vol. 1, p. 113).

18. DeBra, D. B., and J. W. Conklin. "Measurement of drag and its cancellation."Classical and Quantum Gravity 28.9 (2011): 094015.

19. Grynagier, A., Fichter, W., & Vitale, S. (2009). The LISA Pathfinder drift mode: implementation solutions for a robust algorithm. Classical and Quantum Gravity, 26(9), 094007.

20. Conklin, J. W. (2015). Drift mode accelerometry for spaceborne gravity measurements. Journal of Geodesy, 89(11), 1053-1070.

21. Clyde Space, "Small Satellite Reaction Wheels", Jan 2016.

22. Maryland Aerospace Inc., "MAI-400 Reaction Wheel", MAI-000-00010000 datasheet, Jan. 2016.

23. Blue Canyon Technologies, "BCT XACT", BCT XACT datasheet, Jan. 2016.

24. Chilton, A., Shelley, R., Olatunde, T., Ciani, G., Conklin, J. W., & Mueller, G. (2015). The UF Torsion Pendulum, a LISA Technology Testbed: Sensing System and Initial Results. In Journal of Physics: Conference Series (Vol. 610, No. 1, p. 012038). IOP Publishing.

25. Armano, M., Benedetti, M., Bogenstahl, J., Bortoluzzi, D., Bosetti, P., Brandt, N., & Danzmann, K. (2009). LISA Pathfinder: the experiment and the route to LISA. Classical and Quantum Gravity, 26(9), 094001.

26. Bencze, W. J., DeBra, D. B., Herman, L., Holmes, T., Adams, M., Keiser, G. M., & Everitt, C. W. F. (2006). On-orbit performance of the Gravity Probe B drag-free translation control system. In Proc. 29th Guidance and Control Conference. American Astronautical Society, Breckenridge, Colorado.

27. Bhanderi, D. D. (2005). Spacecraft Attitude Determination with Earth Albedo Corrected Sun Sensor Measurements. Department of Control Engineering, Aalborg University.

28. Board, S. S. (2007). Earth Science and Applications from Space: National Imperatives for the Next Decade and Beyond. National Academies Press.

29. Busek Co. Inc., "100μN Electrospray Thruster System", 7008516E datasheet, Jan. 2016.

30. Canuto, E. (2008). Drag-free and attitude control for the GOCE satellite. Automatica, 44(7), 1766-1780.

31. Canuto, E., Molano-Jimenez, A., & Perez-Montenegro, C. (2012). Disturbance rejection in space applications: problems and solutions. Acta Astronautica, 72, 121-131.

32. Cavalleri, A., Ciani, G., Dolesi, R., Heptonstall, A., Hueller, M., Nicolodi, D, and Weber, W. J. (2009). A new torsion pendulum for testing the limits of free-fall for LISA test masses. Classical and Quantum Gravity, 26(9), 094017.

33. Ciani, G. (2008). Free-fall of LISA Test-Masses: a new torsion pendulum to test translational acceleration. Ph.D. Thesis, University of Trento.

34. Christophe, B., Marque, J., & Foulon, B. (2010, December). In-orbit data verification of the accelerometers of the ESA GOCE mission. In SF2A-2010: Proceedings of the Annual meeting of the French Society of Astronomy and Astrophysics (Vol. 1, p. 113).

35. Conklin, J., Balakrishnan, K., Buchman, S., Byer, R., Cutler, G., DeBra, D., & Zoellner, A. (2012). The Drag-free CubeSat.

36. Danzmann, K., & Rüdiger, A. (2003). LISA technology – concept, status, prospects. Classical and Quantum Gravity, 20(10), S1.

37. Drob, D. P., Emmert, J. T., Crowley, G., Picone, J. M., Shepherd, G. G., Skinner, W., & Meriwether, J. W. (2008). An empirical model of the Earth's horizontal wind fields: HWM07. Journal of Geophysical Research: Space Physics, 113(A12).

38. Gerardi, D., Allen, G., Conklin, J. W., Sun, K. X., DeBra, D., Buchman, S., & Johann, U. (2009). Advanced drag-free concepts for future space-based interferometers: acceleration noise performance. arXiv preprint arXiv:0910.0758.

39. Lange, B. (1964). The drag-free satellite. AIAA Journal, 2(9), 1590-1606.

40. Moe, M. M., Wallace, S. D., & Moe, K. (1993). Refinements in determining satellite drag coefficients-Method for resolving density discrepancies.Journal of guidance, control, and dynamics, 16(3), 441-445.

41. Picone, J. M., Hedin, A. E., Drob, D. P., & Aikin, A. C. (2002). NRLMSISE-00 empirical model of the atmosphere: Statistical comparisons and scientific issues. Journal of Geophysical Research: Space Physics, 107(A12).

42. Saulson, P. R. (1990). Thermal noise in mechanical experiments. Physical Review D, 42(8), 2437.

43. Schumaker, B. L. (2003). Disturbance reduction requirements for LISA.Classical and Quantum Gravity, 20(10), S239.

44. Sheard, B. S., Heinzel, G., Danzmann, K., Shaddock, D. A., Klipstein, W. M., & Folkner, W. M. (2012). Intersatellite laser ranging instrument for the GRACE follow-on mission. Journal of Geodesy, 86(12), 1083-1095.

45. Sun, K. X., Allen, G., Buchman, S., Byer, R. L., Conklin, J. W., DeBra, D. B., & Robertson, N. A. (2006, November). Progress in Developing the Modular Gravitational Reference Sensor. In Laser Interferometer Space Antenna: 6th International LISA Symposium (Vol. 873, No. 1, pp. 515-521). AIP Publishing.